

Time-resolved cathodoluminescence microscopy with sub-nanosecond beam blanking for direct evaluation of the local density of states

Moerland, Robert; Weppelman, Gerward; Garming, Mathijs; Kruit, Pieter; Hoogenboom, Jacob

DOI

[10.1364/OE.24.024760](https://doi.org/10.1364/OE.24.024760)

Publication date

2016

Document Version

Final published version

Published in

Optics Express

Citation (APA)

Moerland, R., Weppelman, G., Garming, M., Kruit, P., & Hoogenboom, J. (2016). Time-resolved cathodoluminescence microscopy with sub-nanosecond beam blanking for direct evaluation of the local density of states. *Optics Express*, 24(21), 24760-24772. <https://doi.org/10.1364/OE.24.024760>

Important note

To cite this publication, please use the final published version (if applicable). Please check the document version above.

Copyright

Other than for strictly personal use, it is not permitted to download, forward or distribute the text or part of it, without the consent of the author(s) and/or copyright holder(s), unless the work is under an open content license such as Creative Commons.

Takedown policy

Please contact us and provide details if you believe this document breaches copyrights. We will remove access to the work immediately and investigate your claim.

Time-resolved cathodoluminescence microscopy with sub-nanosecond beam blanking for direct evaluation of the local density of states

ROBERT J. MOERLAND,^{1,2} I. GERWARD C. WEPPELMAN,¹ MATHIJS W. H. GARMING,¹ PIETER KRUIT,¹ AND JACOB P. HOOGENBOOM^{1,3}

¹Department of Imaging Physics, Delft University of Technology, NL-2600 GA Delft, The Netherlands

²r.j.moerland@tudelft.nl

³j.p.hoogenboom@tudelft.nl

Abstract: We show cathodoluminescence-based time-resolved electron beam spectroscopy in order to directly probe the spontaneous emission decay rate that is modified by the local density of states in a nanoscale environment. In contrast to dedicated laser-triggered electron-microscopy setups, we use commercial hardware in a standard SEM, which allows us to easily switch from pulsed to continuous operation of the SEM. Electron pulses of 80–90 ps duration are generated by conjugate blanking of a high-brightness electron beam, which allows probing emitters within a large range of decay rates. Moreover, we simultaneously attain a resolution better than $\lambda/10$, which ensures details at deep-subwavelength scales can be retrieved. As a proof-of-principle, we employ the pulsed electron beam to spatially measure excited-state lifetime modifications in a phosphor material across the edge of an aluminum half-plane, coated on top of the phosphor. The measured emission dynamics can be directly related to the structure of the sample by recording photon arrival histograms together with the secondary-electron signal. Our results show that time-resolved electron cathodoluminescence spectroscopy is a powerful tool of choice for nanophotonics, within reach of a large audience.

Published by The Optical Society under the terms of the [Creative Commons Attribution 4.0 License](https://creativecommons.org/licenses/by/4.0/). Further distribution of this work must maintain attribution to the author(s) and the published article's title, journal citation, and DOI.

OCIS codes: (250.1500) Cathodoluminescence; (260.3800) Luminescence; (020.5580) Quantum electrodynamics; (180.0180) Microscopy; (310.6628) Subwavelength structures, nanostructures.

References and links

1. E. Purcell, "Spontaneous emission probabilities at RF frequencies," *Phys. Rev.* **69**, 681 (1946).
2. G. Grynberg, A. Aspect, and C. Fabre, *Introduction to Quantum Optics: From the Semi-classical Approach to Quantized Light* (Cambridge University Press, 2010).
3. K. H. Drexhage, M. Fleck, F. P. Schäfer, and W. Sperling, "Beeinflussung der Fluoreszenz eines Europium-chelates durch einen Spiegel," *Ber. Bunsenges. Phys. Chem.* **20**, 1176 (1966).
4. K. H. Drexhage, "Influence of a dielectric interface on fluorescence decay time," *J. Lumin.* **1–2**, 693–701 (1970).
5. R. R. Chance, A. H. Miller, A. Prock, and R. Silbey, "Fluorescence and energy transfer near interfaces: The complete and quantitative description of the Eu^{+3} /mirror systems," *J. Chem. Phys.* **63**, 1589 (1975).
6. W. Lukosz and R. E. Kunz, "Light-emission by magnetic and electric dipoles close to a plane interface. I. total radiated power," *J. Opt. Soc. Am.* **67**, 1607–1615 (1977).
7. L. Novotny, "Allowed and forbidden light in near-field optics. I. a single dipolar light source," *J. Opt. Soc. Am. A* **14**, 91–104 (1997).
8. W. L. Barnes, "Fluorescence near interfaces: The role of photonic mode density," *J. Mod. Opt.* **45**, 661–699 (1998).
9. A. P. Alivisatos, M. F. Arndt, S. Efrima, D. H. Waldeck, and C. B. Harris, "Electronic energy transfer at semiconductor interfaces. I. energy transfer from two-dimensional molecular films to Si(111)," *J. Chem. Phys.* **86**, 6540 (1987).
10. I. Pockrand, A. Brillante, and D. Möbius, "Nonradiative decay of excited molecules near a metal surface," *Chem. Phys. Lett.* **69**, 499–504 (1980).
11. R. J. Moerland and J. P. Hoogenboom, "Subnanometer-accuracy optical distance ruler based on fluorescence quenching by transparent conductors," *Optica* **3**, 112–117 (2016).

12. M. Steiner, F. Schleifenbaum, C. Stupperich, A. Virgilio Failla, A. Hartschuh, and A. J. Meixner, "Microcavity-controlled single-molecule fluorescence," *ChemPhysChem* **6**, 2190–2196 (2005).
13. J. P. Hoogenboom, G. Sanchez-Mosteiro, G. Colas des Francs, D. Heinis, G. Legay, A. Dereux, and N. F. van Hulst, "The single molecule probe: nanoscale vectorial mapping of photonic mode density in a metal nanocavity," *Nano Lett.* **9**, 1189–1195 (2009).
14. K. Guo, M. A. Verschuuren, and A. F. Koenderink, "Superresolution imaging of the local density of states in plasmon lattices," *Optica* **3**, 289–298 (2016).
15. R. X. Bian, R. C. Dunn, X. S. Xie, and P. T. Leung, "Single molecule emission characteristics in near-field microscopy," *Phys. Rev. Lett.* **75**, 4772–4775 (1995).
16. J. K. Trautman and J. J. Macklin, "Time-resolved spectroscopy of single molecules using near-field and far-field optics," *Chem. Phys.* **205**, 221–229 (1996).
17. S. Kühn, U. Håkanson, L. Rogobete, and V. Sandoghdar, "Enhancement of single-molecule fluorescence using a gold nanoparticle as an optical nanoantenna," *Phys. Rev. Lett.* **97**, 017402 (2006).
18. M. Frimmer, Y. Chen, and A. F. Koenderink, "Scanning emitter lifetime imaging microscopy for spontaneous emission control," *Phys. Rev. Lett.* **107**, 123602 (2011).
19. S. Kühn, C. Hettich, C. Schmitt, J. P. Poizat, and V. Sandoghdar, "Diamond colour centres as a nanoscopic light source for scanning near-field optical microscopy," *J. Microsc.* **202**, 2–6 (2001).
20. F. J. García de Abajo, "Optical excitations in electron microscopy," *Rev. Mod. Phys.* **82**, 209–275 (2010).
21. N. Yamamoto, K. Araya, and F. J. García de Abajo, "Photon emission from silver particles induced by a high-energy electron beam," *Phys. Rev. B* **64**, 205419 (2001).
22. M. Kuttge, E. J. R. Vesseur, A. F. Koenderink, H. J. Lezec, H. A. Atwater, F. J. García de Abajo, and A. Polman, "Local density of states, spectrum, and far-field interference of surface plasmon polaritons probed by cathodoluminescence," *Phys. Rev. B* **79**, 113405 (2009).
23. K. Takeuchi and N. Yamamoto, "Visualization of surface plasmon polariton waves in two-dimensional plasmonic crystal by cathodoluminescence," *Opt. Express* **19**, 12365–12374 (2011).
24. R. Sapienza, T. Coenen, J. Renger, M. Kuttge, N. F. van Hulst, and A. Polman, "Deep-subwavelength imaging of the modal dispersion of light," *Nat. Mater.* **11**, 781–787 (2012).
25. A. Steckenborn, H. Münzel, and D. Bimberg, "Cathodoluminescence lifetime pattern of GaAs surfaces around dislocations," *J. Lumin.* **24-25**, 351–354 (1981).
26. M. A. Herman, D. Bimberg, and J. Christen, "Heterointerfaces in quantum wells and epitaxial growth processes: Evaluation by luminescence techniques," *J. Appl. Phys.* **70**, R1–R52 (1991).
27. M. Merano, S. Sonderegger, A. Crottini, S. Collin, P. Renucci, E. Pelucchi, A. Malko, M. H. Baier, E. Kapon, B. Deveaud, and J. D. Ganiere, "Probing carrier dynamics in nanostructures by picosecond cathodoluminescence," *Nature* **438**, 479–482 (2005).
28. X. Fu, G. Jacopin, M. Shahmohammadi, R. Liu, M. Benameur, J.-D. Ganière, J. Feng, W. Guo, Z.-M. Liao, B. Deveaud, and D. Yu, "Exciton drift in semiconductors under uniform strain gradients: Application to bent ZnO microwires," *ACS Nano* **8**, 3412–3420 (2014).
29. O. F. Mohammed, D. S. Yang, S. K. Pal, and A. H. Zewail, "4D scanning ultrafast electron microscopy: visualization of materials surface dynamics," *J. Am. Chem. Soc.* **133**, 7708–7711 (2011).
30. L. Tizei and M. Kociak, "Spatially resolved quantum nano-optics of single photons using an electron microscope," *Phys. Rev. Lett.* **110**, 153604 (2013).
31. S. Meuret, L. H. G. Tizei, T. Auzelle, R. Songmuang, B. Daudin, B. Gayral, and M. Kociak, "Lifetime measurements well below the optical diffraction limit," *ACS Photonics* **3**, 1157–1163 (2016).
32. K. Ura, H. Fujioka, and T. Hosokawa, "Picosecond pulse stroboscopic scanning electron microscope," *Journal of Electron Microscopy* **27**, 247–252 (1978).
33. D. Winkler, R. Schmitt, M. Brunner, and B. Lischke, "Flexible picosecond probing of integrated circuits with chopped electron beams," *IBM J. Res. Dev.* **34**, 189–203 (1990).
34. A. Lassise, P. H. Mutsaers, and O. J. Luiten, "Compact, low power radio frequency cavity for femtosecond electron microscopy," *Rev. Sci. Instrum.* **83**, 043705 (2012).
35. D. Poelman and P. F. Smet, "Time resolved microscopic cathodoluminescence spectroscopy for phosphor research," *Physica B* **439**, 35–40 (2014).
36. A. H. V. van Veen, C. W. Hagen, J. E. Barth, and P. Kruit, "Reduced brightness of the ZrO/W Schottky electron emitter," *J. Vac. Sci. Technol. B* **19**, 2038–2044 (2001).
37. A. C. Zonneville, R. F. Van Tol, N. Liv, A. C. Narváez, A. P. Eftting, P. Kruit, and J. P. Hoogenboom, "Integration of a high-NA light microscope in a scanning electron microscope," *J. Microsc.* **252**, 58–70 (2013).
38. A. C. Narváez, I. G. Weppelman, R. J. Moerland, N. Liv, A. C. Zonneville, P. Kruit, and J. P. Hoogenboom, "Cathodoluminescence microscopy of nanostructures on glass substrates," *Opt. Express* **21**, 29968–29978 (2013).
39. Material data provided by manufacturer: CRYTUR, spol. s r.o. <http://www.crytur.cz>.
40. A. C. Narváez, I. G. C. Weppelman, R. J. Moerland, J. P. Hoogenboom, and P. Kruit, "Confocal filtering in cathodoluminescence microscopy of nanostructures," *Appl. Phys. Lett.* **104**, 251121 (2014).
41. E. Zych, C. Brecher, and J. Glodo, "Kinetics of cerium emission in a YAG:Ce single crystal: the role of traps," *J. Phys.: Condens. Matter* **12**, 1947–1958 (2000).
42. W. R. Leo, *Techniques for Nuclear and Particle Physics Experiments : A How-To Approach* (Springer-Verlag, 1987),

- 1st ed.
43. M. Moszyński, T. Ludziejewski, D. Wolski, W. Klamra, and L. O. Norlin, "Properties of the YAG : Ce scintillator," *Nucl. Instrum. Meth. A* **345**, 461–467 (1994).
 44. P. Hovington, D. Drouin, and R. Gauvin, "CASINO: A new monte carlo code in C language for electron beam interaction —part I: Description of the program," *Scanning* **19**, 1–14 (1997).
 45. M. Toth and M. R. Phillips, "Monte Carlo modeling of cathodoluminescence generation using electron energy loss curves," *Scanning* **20**, 425–432 (1998).
 46. L. Novotny and B. Hecht, *Principles of Nano-Optics* (Cambridge University Press, 2006), 1st ed.

1. Introduction

One of the paradigms in nanophotonics is the engineering of the spontaneous emission decay rate of emitters. The spontaneous emission decay rate depends strongly on the local nanoscale environment via the optical local density of states (LDOS) [1], which effectively describes the coupling of light and matter. This is expressed by the Fermi Golden Rule [2]:

$$\gamma = \frac{1}{\tau} = \frac{2\pi}{\hbar} |\langle 2|H_d|1\rangle|^2 \rho(\vec{r}, \omega). \quad (1)$$

Here, γ is the decay rate of the emitter, τ the lifetime, H_d the Hamiltonian pertaining to the transition from state $|2\rangle$ to state $|1\rangle$ in the electric dipole approximation, and $\rho(\vec{r}, \omega)$ the LDOS. In the early 1960s, a range of experiments were conducted that in the optical regime unequivocally established the relation between the decay rate and the local (stratified) environment of an emitter [3, 4]. Intrinsically a quantum-mechanical entity, it turns out that the *relative* LDOS = γ/γ_0 can be calculated with classical dipoles, where γ_0 is the decay rate in a reference environment [5–8]. Since then, various schemes to measure the decay rate on the nanoscale have been published, such as using spacers to control emitter-to-structure distance [9–11], dispersing molecules to map the spatially-resolved LDOS of a single structure [12–14], scanning a nanoscale structure over a single emitter [15–17] and scanning emitters embedded in scanning-probe geometries over a (nano)structure [18, 19].

Cathodoluminescence (CL) microscopy is a powerful technique to probe structural heterogeneity in material properties, typically by intensity or spectral contrast. Recently, CL has gained interest in the field of nanophotonics, where the connection between the LDOS and the intensity of coherent transition radiation, induced by the electron beam [20], has been used to infer the LDOS in various metal and silicon structures far below the optical diffraction limit [21–24]. This method, however, is limited by the incoherent background that is induced simultaneously. A direct evaluation of the LDOS through measurement of excited state lifetimes of active emitters has so far not been demonstrated using CL. Scanning probe optical techniques can be used for sub-wavelength resolution [18, 19] but scanning a fragile probe over the sample surface can be cumbersome and, moreover, the interaction is limited to the surface. The latter is particularly problematic when the surface is highly reflective. CL lifetime microscopy would allow direct measurement of the LDOS even underneath such a reflecting surface, but requires a pulsed electron beam.

In the past, pulsed electron beams have been used to investigate structural disorder in arsenide-based quantum well heterostructures at micron-scale resolution [25, 26]. More recently, dedicated laser-triggered electron sources have allowed to reveal carrier dynamics at the nanoscale and with picosecond time resolution in GaAs and ZnO nanostructures [27, 28]. Also surface dynamics in semiconductor materials has been investigated in this way [29]. Alternatively, with continuous-beam STEM, a Hanbury-Brown-Twiss (HBT) CL detection scheme has been used to demonstrate photon anti-bunching in nanodiamond nitrogen vacancy centers [30] and to measure excited state lifetime variations in separated single quantum wells [31].

Contrary to the other modes of CL analysis, which can be performed with custom inserts or retrofits on standard SEMs, CL lifetime microscopy with laser-triggered electron sources

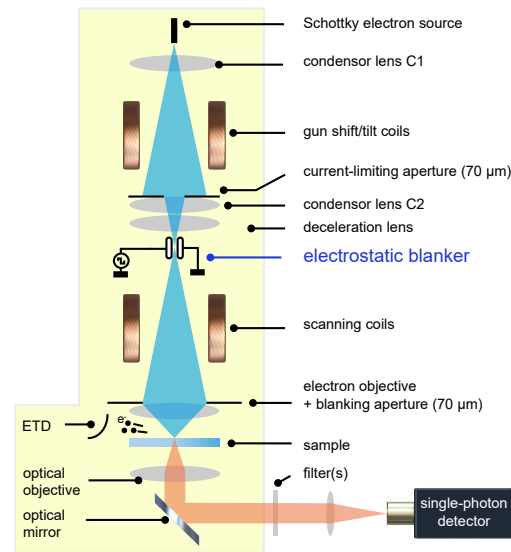


Fig. 1. Experimental setup to measure time-resolved cathodoluminescence. All elements within the yellow boundary are placed inside the vacuum of a Scanning Electron Microscope (SEM). At the top, a Schottky source provides the electrons that make up the electron beam. Condenser lens C1 is used to set the current in the electron beam. The combination of the condenser lens C2 and the deceleration lens is modified such, that it focuses the electron beam in between the blower plates. Finally, the electron objective lens images this focus onto the sample. Since the two foci are conjugated, the beam remains stationary while blanking; see Fig. 2. Simultaneously, secondary electrons are detected by an Everhart-Thornley Detector (ETD).

requires drastic modification of the SEM and hampers switching between pulsed and continuous beam operation, e.g., for alignment and every-day device inspection. Moreover, the low effective current in the pulsed beam may be a drawback. Beam blanking [32–35] provides an alternative that maintains the high brightness of, e.g., Schottky sources [36], with flexibility in the choice of pulse duration and repetition rate as a benefit. Furthermore, there is no need for addition of a pulsed laser. However, for application of lifetime CL in nanophotonics both temporal and spatial resolution need to be ‘sufficient’, i.e., far below the diffraction limit and far below typical emitter lifetimes respectively. To our knowledge, in all beam-blanking based approaches reported to date, these two requirements have not been met simultaneously. Here, we demonstrate time scales typical for commonly-used pulsed laser diodes, i.e., tens of picoseconds, and a spatial resolution that is in the range of optical near-field techniques. We demonstrate that deep-subnanosecond beam blanking in conjunction with time-resolved CL photon detection can be implemented using standard SEM hardware and electronics, while simultaneously reaching a $\lambda/10$ spatial resolution. To illustrate the application of time-resolved CL in nanophotonics, we present the results of an experiment that probes LDOS-induced excited state lifetime modifications of phosphors across and underneath a sharp aluminum edge.

2. Setup, blanking technique and resolution in time and space

In Fig. 1, a diagram of our setup is shown. We use a standard commercial beam blower (FEI), which is inserted into the column of a FEI Quanta FEG 200 SEM. For CL collection, we have inserted an inverted light microscopy stage with a $60\times$ optical objective with an NA of 0.95 (Nikon) [37, 38]. As a detector we use an avalanche photodiode, capable of single-photon

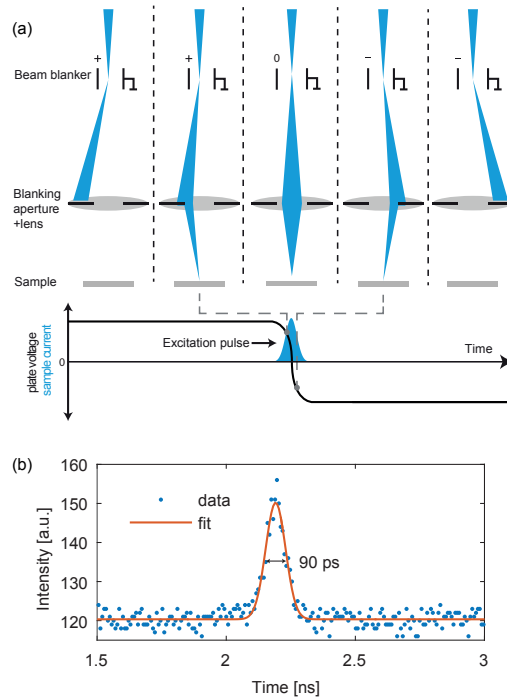


Fig. 2. Depiction of conjugate beam-blanking in order to create electron pulses. (a) At $t = 0$, the electron beam is angularly deflected and fully blanked by an aperture at the location of the electron lens. Reversing the voltage across the blankeer plates scans the electron beam over the aperture. As long as the beam is not fully blanked, electrons will be focused onto the sample. Therefore, by swiftly inverting the voltage, an electron pulse is delivered to the sample in the focus. The pulse length was characterized with a custom-built streak camera (see Sec. A.1 in the appendix). (b) A fit with Gaussian profile yields a 90 ps pulse length full-width at half the maximum. The non-zero baseline is due to the dark current of the camera.

counting (PicoQuant). The beam blankeer is driven with a generic pulse generator, which also provides the required synchronization to implement a time-correlated single-photon counting scheme (PicoQuant PicoHarp 300).

We adjust the electron lenses such that the first crossover occurs between the blankeer plates of the electrostatic beam blankeer, conjugate to the beam focus on the sample [33]. In that case, when a voltage difference is applied to the blankeer plates, the result is an angular change of the electron beam only. The virtual source of the electrons, i.e., the crossover between the blankeer plates, remains stationary. Therefore, the location of the electron beam on the sample is stationary too, paramount for high-resolution imaging. An aperture with a diameter of $70 \mu\text{m}$, inserted close to the pivot point of the final electron lens, ensures that a small voltage difference across the plates is sufficient to fully blank the beam while also minimizing the influence of aberrations. Thus, by sweeping the electron beam across the aperture, pulses of electrons are generated and subsequently focused onto the sample (see Fig. 2(a)).

2.1. Pulse length

With a custom-made streak-camera (see section A.1 in the appendix), we determine the upper limit of the pulse length to be as low as 90 ps (see Fig. 2(b)), where our measurement is limited by the jitter in the pulse generator (E-H Research Laboratories 137, specified minimum rise

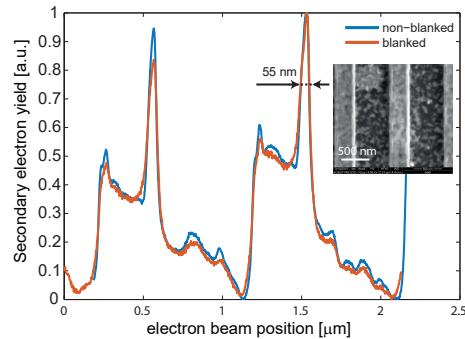


Fig. 3. Scanning Electron Microscope resolution with the electron beam in continuous (blue curve) and pulsed (red curve) mode. A substrate containing tungsten and chromium strips is used as a test sample (see inset). After an image is obtained, the secondary-electron signal is integrated along the vertical axis (parallel to the strips), which results in the two curves shown. All features of the sample are faithfully reproduced in pulsed mode

time 0.5 ns/V, Sec. A.1). This is of a similar length as typical commercially-available pulsed diode lasers, and therefore is suitable to excite many types of luminescent materials. Pulses of ≤ 350 ps can still be obtained with a pulse generator with a more moderate rise time of 6 ns/V such as the Philips PM 5715. A longer pulse leads to larger optical and secondary-electron (SE) signals, as the average current increases. Therefore, we choose to use the longer pulse length in the following. Still, the pulse length is much shorter than the nanosecond timescale of the process we use for our proof of principle below [39].

2.2. Spatial resolution

By setting the blanker voltage to zero, the SEM can be switched from pulsed to continuous beam operation. We use this to establish that SEM performance is similar in both modes. We image an Yttrium-Aluminum-Garnet (YAG) substrate containing a regular pattern of chromium and tungsten strips (see inset in Fig 3). First, we image the sample with the SEM in continuous mode at 4 kV with a current of 20 pA, while measuring the secondary-electron (SE) signal. The SEM is configured in conjugated mode, i.e., the crossover is placed between the blanker plates, but the blanker is not used. Next, we image the same area again, but this time we drive the beam blanker with the pulse generator operating at 50 MHz, with a 50% duty cycle. Afterwards, we integrate the SE signal in the vertical direction, parallel to the tungsten lines and plot the result for both acquisitions, after normalizing to the maximum value. The result is shown in Fig. 3, where the blue curve is the result without blanking, and the red curve is the result of imaging with electron pulses. From this data we conclude that also when pulsing the electron beam, all the features of the original image are faithfully reproduced. The main difference is the somewhat higher noise level in the image taken in pulsed mode, which is due to the effectively lower current that probes the sample. Note that the displacement of the first crossover in the SEM adversely affects the spatial resolution, which explains the somewhat lower continuous-beam resolution than what might be expected for normal (unconjugated) operation. Furthermore, the SEM used here does not have a magnetic immersion mode, which further limits the resolution at lower energies.

3. Photonics application: decay rate modification due to local density of states

We illustrate the application of time-resolved cathodoluminescence by directly probing the excited-state lifetime of Ce^{3+} as a function of distance to a metal mirror with $\lambda/10$ precision,

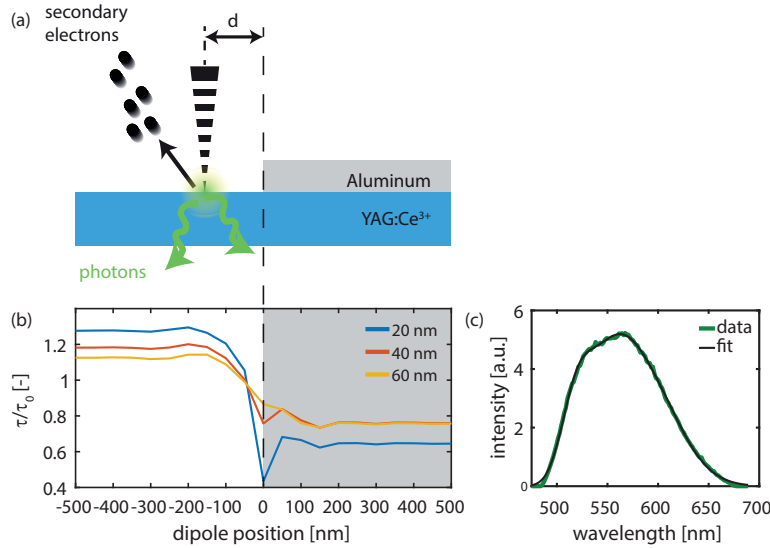


Fig. 4. Resolving excited-state dynamics with a pulsed electron beam. (a) A Ce³⁺:YAG sample is covered by half with aluminum and scanned through a pulsed electron beam. The electronic excitation results in emission of photons and the generation of secondary electrons. By recording both as a function of d , we can directly correlate the local structure of the sample with the decay dynamics. (b) A finite-difference time-domain simulation yields an estimate of the change in (orientationally averaged) lifetime as a function of distance d . The lifetime is normalized with the lifetime in solid Ce³⁺:YAG and weighted by the emission spectrum of cerium in a YAG host (see panel (c)). Negative values on the x -axis mean excitation on the uncoated Ce³⁺:YAG, and positive values mean excitation underneath the aluminum. To account for the (energy-dependent) electron penetration depth, we simulate the relative lifetime at several depths (20, 40 and 60 nm). (c) Measured emission spectrum of Ce³⁺:YAG (green curve). Excitation was with electrons of 4 keV energy. The black curve is a fit with three Gaussian distributions.

where $\lambda = 567$ nm is the peak emission wavelength of Ce³⁺. The experiment is schematically indicated in Fig. 4(a). A YAG substrate doped with Ce³⁺ ions (Crytur) is covered by half with a 30 nm layer of aluminum. The sample is scanned through the pulsed electron beam with a piezo translation stage. We keep the electron beam stationary in order to maintain the electron beam focus conjugate to the opening aperture of the photodiode [40]. We record the arrival times of photons that are the result of the electronic excitation by the electron beam, as a function of the distance d of the beam to the aluminum edge. Simultaneously, we record the SE signal. Therefore, we can directly correlate the observed decay dynamics to the structure of the sample.

To get an estimate of the change in lifetime, finite-difference time-domain simulations are performed (Lumerical) for emitters at a certain distances to the aluminum edge. Here, we assume an isotropic emitter, and average the change in lifetime over emitter orientation. The lifetimes are normalized with the lifetime in solid Ce³⁺:YAG and weighted by the emission spectrum of cerium in a YAG host:

$$\frac{\tau}{\tau_0} = \left[\int_0^\infty \frac{1}{3} (\hat{\rho}_x(\vec{r}, \omega) + \hat{\rho}_y(\vec{r}, \omega) + \hat{\rho}_z(\vec{r}, \omega)) S(\omega) d\omega \right]^{-1}, \quad (2)$$

where $\hat{\rho}_{x,y,z}(\vec{r}, \omega)$ is the frequency- and location-dependent relative LDOS for x -, y - and z -oriented dipoles, and $S(\omega)$ is the normalized emission spectrum of Ce³⁺:YAG with

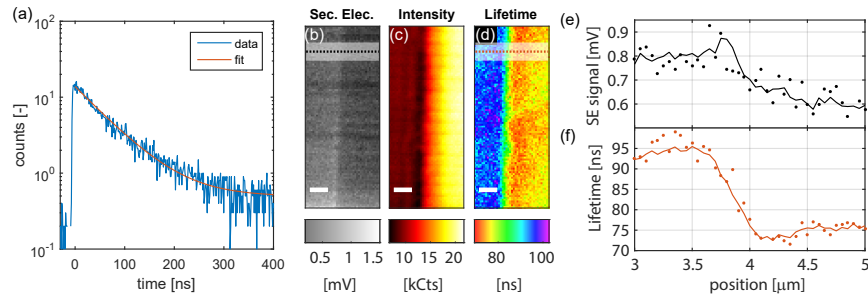


Fig. 5. Measurement results of a YAG sample containing Ce^{3+} , coated with aluminum on one side. (a) An example of the measured decay curve of Ce^{3+} in YAG. The red curve is a fit with the model $\exp(-\gamma t) + C$, which is a reasonably accurate representation of the data. The lifetime τ is then obtained from $\tau = 1/\gamma$. (b) Secondary-electron signal. The darker side depicts the sample side coated with aluminum. (c) Cerium emission intensity. (d) Cerium lifetime. Scale bar is 500 nm. (e) Cross section of an average of 10 scan lines of the secondary-electron signal (solid curve), and the data from a single line scan (dots), corresponding to the highlighted area and dotted line in (b), respectively. We refrain from averaging over all scan lines in order to limit the impact of the slight rotation that the sample has with respect to the y -axis. (f) Cross section of the lifetime of cerium emission, averaged over 10 line scans (solid curve) and the data from a single line scan (dots), corresponding to the highlighted area and dotted line in (d), respectively.

$\int_0^\infty S(\omega)d\omega = 1$. Furthermore, the penetration depth of electrons is taken into account by simulating dipole emitters at several depths. The result of this simulation is shown in Fig. 4(b). Coming from the uncoated side of sample, the lifetime drastically reduces close to the aluminum edge. Passing the edge and going further under the aluminum, the lifetime recovers slightly but remains shorter than for uncoated Ce^{3+} :YAG. This is in accordance with emission near infinitely large metal and dielectric interfaces, respectively. See also Sec. A.2 in the appendix. Finally, a measured emission spectrum of Ce^{3+} :YAG is displayed in Fig. 4(c), together with a fit with three Gaussian distributions that after normalization yields $S(\omega)$. We note that our experiment will probe emitters throughout the electron interaction volume, convoluting the simulation results with the excitation probability distribution for a given electron energy. Therefore, we choose to operate at a relatively low electron energy of 4 keV.

The experiment is performed with a pulse frequency of about 500 kHz, which causes an electron pulse being generated every $1 \mu\text{s}$ (two per period). This leads to an effective current of approximately $20 \text{ pA} \times 10^6/\text{s} \times 0.35 \text{ ns} = 7 \text{ fA}$. The sample is stepped with a step size of 50 nm in the x - and y -direction. At every sample location, we measure the SE signal and the arrival histogram of the cerium photons with a dwell time of 3 seconds, leading to a total acquisition time of just over 4 hours for the $2 \times 6 \mu\text{m}^2$ area. A bandpass filter with a center wavelength of 542 nm and a width of 20 nm is used to prevent pile-up during time-correlated single-photon counting. Note that this does not affect the lifetime measurement, as the $4f$ to $5d$ transition of the cerium ion probes the LDOS over its entire spectrum [41].

It is well-known that electronic stimulation of scintillator materials such as Ce^{3+} :YAG typically results in decay curves that are at least bi-exponential [42]. However, the connection between the number of exponents and the physical meaning is lost [41]. Here, for sake of simplicity, we fit our data with a single exponential decay in order to focus on the change in decay rate of the cerium emitter due to the change in LDOS, instead of on the complex decay dynamics of scintillators. Moreover, our data can be reproduced reasonably well with a single exponential decay, see Fig. 5(a), implying that there is a single physical decay channel that is dominant [41, 43]. The

results of this measurement are shown in Fig. 5(b–d). The SE signal is shown in Fig. 5(b). Here, the darker part of the graph depicts the area covered with aluminum (lower SE yield than YAG). The measured cerium emission intensity is shown in Figure 5(c). The intensity was obtained by summing all the photon counts in the recorded arrival time histogram. Finally, in Fig. 5(d), we show the lifetime — based on a single exponential decay — as a function of location. Clearly, as the location of excitation by the electron beam gets closer to the edge of the aluminum, the Ce^{3+} lifetime drops from about 95 ns to 75 ns over a distance of about 500 nm. This can be seen as well in the cross sections shown in Fig. 5(e–f). The lifetime is the shortest near the aluminum edge, and then seems to slightly recover. However, based on the shape of the curve describing lifetime as a function of position (cf. Fig 4(b)), we estimate that most of the CL is generated by electrons that scatter at a depth of around 40–60 nm from the point of entry. This estimation is supported by a Monte-Carlo simulation of the elastic scattering of electrons inside a stack of aluminum and YAG (CASINO) [44,45], which yields a penetration depth, weighted by deposited energy, of 40 and 48 nm into the YAG host crystal, with and without the aluminum layer, respectively. In Sec. A.3 of the appendix we show the results of this simulation.

4. Conclusion

In conclusion, we have demonstrated the generation of electron pulses from a continuous, high-brightness electron source by beam blanking with commercially-available hardware. We achieve a pulse length of 90 ps full-width half-max. This allows a novel type of time-resolved cathodoluminescence microscopy for nanophotonics, by measuring photon arrival times after excitation by electron pulses. The measured excited state lifetimes are correlated to the structure of the sample by recording the secondary-electron signal simultaneously. Our proof-of-principle results illustrate that time-resolved cathodoluminescence is an attractive tool to probe dynamics in photonic nanostructures with high spatial resolution.

A. Appendix

A.1. Pulse duration measurement

The pulse duration was measured using a streak camera, which is a second deflector positioned in between the aperture in the final electron lens and the sample. A metal-covered Yttrium-Aluminum-Garnet (YAG) screen is used as sample, and generated cathodoluminescence (CL) is imaged with a CCD camera.

By rapidly deflecting the electron beam with the second deflector as the electron pulse arrives, the temporal profile of the pulse is converted to a spatial profile on the YAG screen. To ensure proper timing, the streak camera signal is triggered by the blanker signal. The profile on the screen is captured on a long-exposure CCD image, comprising many pulses for adequate luminous intensity. This imaged profile is a convolution of the pulse, the optical point spread function (PSF), and the jitter, all of which are considered Gaussian. Their convolution, i.e. the profile, is then also a Gaussian with width $\sigma_{profile}^2 = \sigma_{pulse}^2 + \sigma_{PSF}^2$. This relation is used to compute the Gaussian width of the pulse after fitting a Gaussian to the profile.

Conversion from the spatial to the temporal domain is performed by making two recordings, where the pulse is delayed by 0.5 ns in the second measurement. For the pulse delay, a Stanford Research Systems DB64 coaxial delay instrument is used. The delay time is verified using a PicoHarp 300 (PicoQuant). By relating the spatial separation of the pulses on the screen to this temporal separation, a conversion factor is found.

First, the time duration of the delay was verified using the PicoHarp 300. Arrival times of pulses from a pulse generator connected to the PicoHarp via the delay instrument were measured with and without a 0.5 ns delay, with a resolution of 4 ps. The results are shown in Fig. 6. The difference in arrival times was found to be 508 ± 6 ps. However, as can be seen in Fig. 6, there is

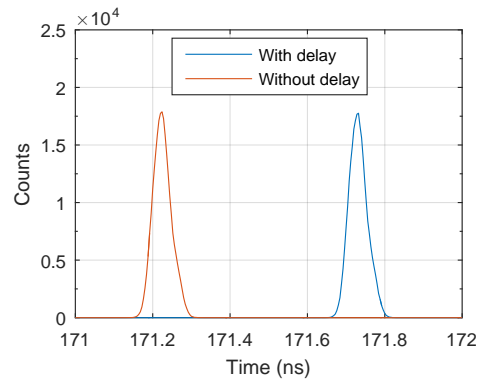


Fig. 6. Arrival times of pulses with and without a set time delay of 0.5 ns. The duration of the delay is measured to be 508 ± 6 ps.

a significant spread in the arrival times, indicating the presence of jitter. The exact magnitude of the jitter cannot be determined from the data, as the jitter in the PicoHarp instrument is not precisely known, but it is specified to be less than 11 ps. Therefore, we conclude that our pulse generator is the main source of jitter.

Then, the quality of the optical focus is assessed. A CCD image of the CL generated by a stationary electron beam is recorded (see inset in Fig. 7(a)), and a line profile of the spot is fitted to a Gaussian function $y = A \exp(-(x - x_0)^2)/(2\sigma^2)) + B$. The resulting fit is shown in Fig. 7(a), and yields $\sigma_{PSF} = 3.65 \pm 0.1$ pixels (95% confidence), corresponding to a full-width at half the maximum (FWHM) of 8.60 pixels.

Next, the pulse recordings are captured. To this end, a 10 V peak-peak square wave is applied to the streak camera, without line termination (ie., open end). To the fast blanker, a 5 V peak-peak square wave is applied, also without line termination. By triggering the streak camera signal with the blanker signal, and tuning the delay, the electron pulse is made to arrive as the streak camera is deflecting the beam from one side to the other. An image is captured with the CCD camera, after which the 508 ps delay is introduced on the fast blanker signal. Subsequently another image is recorded. As a result of this delay, the pulse in the second image is shifted with respect to the first.

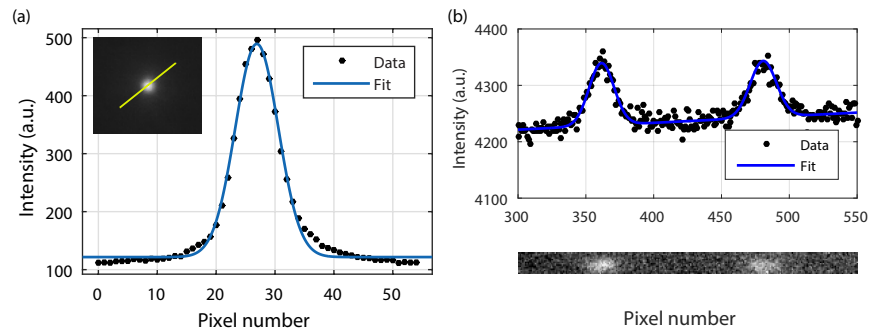


Fig. 7. (a) Line profile of the optical spot (see inset) along the yellow line. The Gaussian fit shows 8.60 pixel FWHM. (b) Intensity profile of the two spots (0.5 ns temporal separation) recorded without line termination on the fast blanker with a double Gaussian fit. The spatial separation between the two pulses is found to be 119.3 pixels, and the average pulse width is 22.2 pixels FWHM.

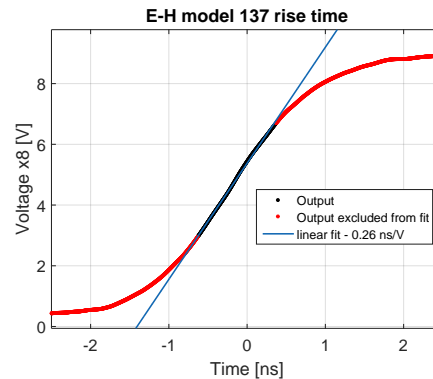


Fig. 8. Measured pulse rise time of the E-H Research Laboratories model 137 pulse generator. Here, the load is $1\text{ M}\Omega\parallel 17\text{ pF}$ at the end of approximately 3 meters of BNC cable ($Z = 50\ \Omega$). The pulse generator was set at 10 MHz with an $8\times$ attenuation.

The two images are added, and a line profile along the direction of deflection is constructed. Two Gaussians are fitted to the line profile, as seen in Fig. 8. The fit positions the maxima at pixel nr. 361.5 and 480.8 (uncertainty 0.7 pixels, 95% confidence), resulting in a deflection of 119.3 ± 1 pixels. The Gaussian widths are 9.21 and 9.66 pixels, respectively, with 0.7 pixel uncertainty, resulting in an average width of 9.43 ± 0.5 pixels, or 22.2 pixels FWHM. Deconvolution with the optical spot gives a width of 8.69 pixels (20.5 pixels FWHM). The 119.3 pixel shift between the two peaks corresponds to a 508 ps delay, so every pixel represents 4.26 ps. Hence, the (jitter-limited) pulse duration here is 87 ± 5 ps.

The generator used to create the pulses shown above is an E-H Research Laboratories model 137, which has a specified minimum rise time of 0.5 ns/V into a $50\ \Omega$ load. However, the pulse generator was used to drive the blanker without termination, i.e., open-ended. In order to estimate the performance of the generator, we measure the rise time of the generator with a Lecroy Waverunner 640Zi, while approximating the open-ended behavior with the $1\text{ M}\Omega\parallel 17\text{ pF}$ input impedance of the oscilloscope at the end of approximately 3 meters of BNC cable ($Z = 50\ \Omega$). The frequency on the pulse generator was set to 10 MHz with $8\times$ attenuation. The result of this measurement yields a 10%–90% rise time of 0.37 ns/V, and a maximum slope of 0.26 ns/V (see Fig. 8).

A.2. Lifetime near vacuum and aluminum interfaces

In order to compare the trend of the numerical results shown in Fig. 4(b) with analytical results, valid far away from the aluminum edge, we calculate the lifetime of an emitter as a function of distance to an interface [5, 46]. In the following, the lifetime is normalized with the lifetime of an emitter in an infinite YAG host crystal. In Fig. 9 the results of this calculation are shown, where we assume an isotropic emitter, i.e., we plot the relative lifetime after averaging over emitter orientation. The plot shows that, for the range of 20–60 nm considered in the main text, the lifetime of the emitter is always shorter when the YAG is covered with aluminum than when the interface is only with vacuum. The shorter lifetime of the emitter underneath aluminum corresponds to the presence of additional decay pathways in the form of, e.g., surface plasmon polaritons or Joule heating [9–11], whereas the longer lifetime near vacuum corresponds to the decrease of pathways for the emitter to decay into [46].

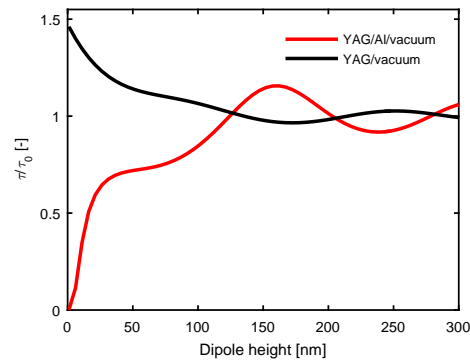


Fig. 9. Calculated relative lifetime of an isotropic emitter inside a YAG host crystal ($n = 1.83$, $\lambda = 542$ nm), as a function of distance to an interface. The case of an interface with vacuum is depicted by the black solid curve, whereas the red solid curve depicts the situation where the YAG has an additional coating of 30 nm-thick aluminum ($n = 0.94 + 6.32i$).

A.3. Electron penetration depth simulation

In order to estimate the generation of cathodoluminescence (CL) as a function of electron scattering, a Monte Carlo simulation is performed (CASINO) [44]. Two cases are considered. In the first case, a semi-infinite half space is filled with Yttrium-Aluminum Garnet ($\text{Y}_3\text{Al}_5\text{O}_{12}$, YAG), with the other half being vacuum. In the second case, the YAG material is covered with an additional layer of aluminum. The standard material properties of aluminum, as present within the CASINO program, are used. For the material properties of YAG, the manufacturer-supplied data of 4.57 g/cm³ is used for the density. An amount of 100,000 electrons with a starting energy of 4 keV is simulated, where the electron injection profile is a Gaussian beam with a width of 40 nm. After the simulation, the trajectories are exported for further processing in MATLAB.

By approximation, the amount of CL is thought to be proportional with the energy lost during elastic scattering [45]. Therefore, during post processing, we consider a volume V , divided into cubes with sides of 5 nm, and determine for every cube the total energy loss inside that subvolume of V . A three-dimensional contour plot of the resulting volume of energy $E_{\text{loss}}(x, y, z)$ is shown in Fig. 10(a) for the first case of only the YAG host material. The contour lines indicate where 10% to 100%, in steps of 10%, of the maximum energy loss occurs, where the maximum energy loss is defined as $\max_V (E_{\text{loss}}(x, y, z))$. The relative electron energy loss as a function of depth is displayed in Fig. 10(b). The typical penetration depth, weighted by the energy loss fraction, turns out to be 48 nm for the YAG host crystal.

A second simulation is run under identical conditions for the case where the YAG crystal is covered with a 30 nm-thick layer of aluminum. Figure 10(c) depicts the energy-loss volume for this particular case, with the same meaning attached to the contour lines as in the previous case. The relative electron energy loss as a function of depth is displayed in Fig. 10(d). Here, the typical penetration depth, weighted by the energy loss fraction, is 59 nm for the combination of aluminum and YAG crystal. However, since the cerium emission stems from the YAG crystal only, the weighted penetration depth excluding the aluminum layer is 40 nm into the YAG host.

Funding

The Netherlands Organization for Fundamental Research (NWO); Foundation for Fundamental Research on Matter (FOM) (10PR2826); Technische Universiteit Delft.

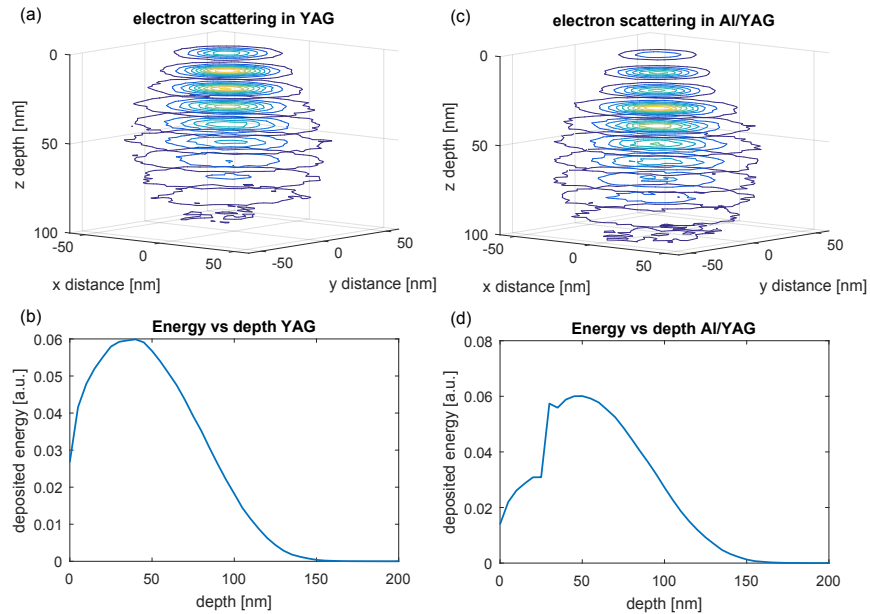


Fig. 10. (a–b) Monte-Carlo simulation (CASINO) of electron scattering in a YAG crystal. In (a), the volume that contains 50% of the energy lost due to elastic scattering is shown. The contour lines indicate 10%, 20% . . . 100% of the maximum energy loss. In (b), the fraction of electron energy loss as a function of depth is plotted. The penetration depth, weighted by the loss fraction, is 48 nm for YAG. (c–d) Monte-Carlo simulation (CASINO) of electron scattering in a YAG crystal, coated with 30 nm of aluminum. In (c), the volume that contains 50% of the energy lost due to elastic scattering is shown. The contour lines indicate 10%, 20% . . . 100% of the maximum energy loss. In (b), the fraction of electron energy loss as a function of depth is plotted. The penetration depth, weighted by the loss fraction, is 59 nm starting from the top of the aluminum layer. However, since the cerium emission stems from the YAG crystal only, the weighted penetration depth excluding the aluminum layer is 40 nm into the YAG host.

Acknowledgments

The authors thank Pim van Dorp for his initial work on the time-resolved electron microscopy setup, and Victor Hartong for his assistance with measuring rise times.

Competing Interest: Our integrated microscope and cathodoluminescence detection set-up served as a prototype for a product by Delmic BV. PK and JPH are co-founders and shareholders in Delmic.